

# High-Resolution Motion-Robust Diffusion-Weighted Imaging with Self-Gated Zero-Shot Self-Supervised Reconstruction

Zhengguo Tan, Patrick A Liebig, Annika Hofmann, Frederik B Laun, Florian Knoll

**Abstract**— This work introduced a self-gated zero-shot self-supervised learning (ZSSL) reconstruction framework for navigator-free, high-resolution diffusion-weighted imaging using undersampled multi-shot interleaved echo-planar imaging (iEPI) acquisition. ZSSL belongs to the algorithm unrolling technique, with a physics-guided data-consistency term and a learned regularization function. We unrolled the alternating direction method of multipliers (ADMM) with a residual neural network to leverage redundancy across the spatial-diffusion-dimension. First, we compared the proposed self-gated ZSSL to conventional methods including parallel imaging as multiplexed sensitivity-encoding (MUSE) and compressed sensing reconstruction with locally-low rank (LLR) regularization. ZSSL supplied excellent reconstruction results in both 4-shot fully-sampled data and 2-shot undersampled data at 1.0 mm isotropic resolution. Second, we demonstrated the capability of self-gated ZSSL in DWI reconstruction with the b-value of 3000 s/mm<sup>2</sup>. Compared to LLR, ZSSL provided more noise reduction and clearer diffusion contrast. Third, self-gated ZSSL was validated with both retrospectively and prospectively acquired data at 0.7 mm isotropic resolution. This approach outperformed both MUSE and LLR regularized reconstruction in terms of image sharpness and motion robustness. While ZSSL required up to eight hours training time per slice, it generalized well to all other slices, with an inference time of just one minute. In comparison, LLR required about two hours per slice. Overall, self-gated ZSSL enables undersampled multi-shot iEPI acquisition without the need of navigators, providing sub-millimeter DWI at clinically feasible reconstruction times. The code is publicly available at: <https://github.com/ZhengguoTan/DeepDWI>.

**Index Terms**— Diffusion weighted imaging, Magnetic resonance imaging, Image reconstruction, End-to-end learning in medical imaging, Machine learning

## I. INTRODUCTION

HIGH-dimensional magnetic resonance imaging (HD-MRI) has been a flourishing field, focused on the acquisition, reconstruction and analysis of multi-dimensional multi-contrast-weighted MRI data. Examples of HD-MRI include but are not limited to magnetic resonance spectroscopic imaging (MRSI) [1], diffusion-weighted imaging (DWI) [2], [3], and quantitative parameter mapping [4], [5]. Conventional HD-MRI, however, requires long acquisition times, making the data susceptible to subject motion and system imperfections, and imposing high computational burden. DWI, in particular, poses challenges in the pursuit of high spatial, temporal, and angular resolution. DWI is typically acquired using the pulsed gradient spin echo sequence [6] followed by fast echo-planar imaging (EPI) readouts [7]. However, the use of long echo trains in EPI results in geometric distortion artifacts and reduced spatial resolution. Additionally, acquiring multiple diffusion directions to enhance angular resolution and to better probe tissue microstructure further extends the scan time.

Advances in parallel imaging [8]–[12] and compressed sensing [13]–[15] have enabled accelerated acquisition for HD-MRI. Notably, the low-rank model [16] has been a powerful tool in dimension reduction. Typically, singular value decomposition (SVD) is used to learn a truncated temporal basis function from a large-scale physics-informed dictionary [17]–[19]. The temporal basis function is then integrated with the MRI forward model, i.e. the sensitivity encoding operator [11], for joint reconstruction of the corresponding spatial basis images. In addition, low-rank regularization can be employed in the joint reconstruction [20].

Beyond the low-rank technique, advanced neural networks, e.g. autoencoder [21], have been explored for HD-MRI reconstruction and proven to supply more accurate representations of high-dimensional data than SVD. Lam et al. [22] and Mani et al. [23] proposed to first learn a denoising autoencoder (DAE) model from a physics-informed simulated dictionary and then incorporate the learned DAE model as a regularizer in the alternating direction method of multipliers (ADMM) [24] unrolling reconstruction. Pioneered by Gregor and LeCun

This work was supported in part by German Research Foundation (DFG) under projects 513220538 and 512819079, project 500888779 in the Research Unit RU5534 for MR biosignatures at UHF, and by the National Institutes of Health (NIH) under grants R01EB024532 and P41EB017183. In addition, scientific support and HPC resources were provided by the Erlangen National High Performance Computing Center (NHR) of Friedrich-Alexander-University Erlangen-Nuremberg (FAU) under the NHR project b143dc. NHR is funded by federal and Bavarian state authorities. NHR@FAU hardware is partially funded by DFG under project 440719683. (*Corresponding Author:* Zhengguo Tan)

Z. Tan was with the Department Artificial Intelligence in Biomedical Engineering (AIBE), FAU, Erlangen, Germany. He is now with the Michigan Institute for Imaging Technology and Translation (MIITT), Department of Radiology, University of Michigan, Ann Arbor, MI 48109 USA (e-mail: zgtan@med.umich.edu).

P. A. Liebig is with Siemens Healthcare GmbH, Erlangen, Germany (e-mail: patrick.liebig@siemens-healthineers.com).

A. Hofmann is with the Department AIBE, FAU, Erlangen, Germany (e-mail: annika.ah.hofmann@fau.de).

F. B. Laun is with the Institute of Radiology, University Hospital Erlangen, FAU, Erlangen, Germany (e-mail: Frederik.Laun@uk-erlangen.de).

F. Knoll is with the Department AIBE, FAU, Erlangen, Germany (e-mail: florian.knoll@fau.de).

[25], algorithm unrolling enables the use of learned deep *priors* as regularization and offers faster inference compared to iterative reconstruction methods that rely on hand-crafted regularization functions [26]. Algorithm unrolling has been applied to accelerated MRI reconstruction in various scenarios: including but not limited to supervised learning with fully sampled reference images [27], [28], and self-supervised learning with only undersampled data available for training [29], [30]. Notably, acquiring fully sampled DWI for training a regularization function is quite challenging. First, fully-sampled DWI requires longer echo times in EPI, which both elongates the scan times and increases off-resonance-induced geometric distortions. Second, the variety of diffusion acquisition modes necessitates a larger dataset compared to two-dimensional imaging scenarios [31]. As a result, self-supervised learning is better suited for DWI reconstruction.

Deep neural networks are capable of learning not only regularization functions, but also MR-physics forward operators. Liu et al. [32] proposed the reference-free  $T_1$  parameter maps extraction (RELAX) self-supervised deep learning reconstruction, which learns the mapping from  $T_1$  parameter maps to undersampled multi-coil multi-contrast  $k$ -space data. Arefeen et al. [33] proposed to replace the conventional SVD-based linear subspace modeling [17] by the latent decoder model within DAE for improved  $T_2$ -weighted image reconstruction. The ability of DAE to learn DWI models is somewhat uncertain. DAE is composed of sequential fully connected layers with nonlinear activation functions, which may struggle with complex functions like those required for DWI signals. For instance, the standard diffusion tensor model [34] consists of six tensor elements, and generates DWI signals based on the multiplication of exponential functions, a process that may be too intricate for simpler architectures to capture effectively.

#### *Contributions:*

- We unrolled ADMM to perform zero-shot self-supervised learning (ZSSL) and incorporated self-gated shot-to-shot phase variation estimation into ZSSL for deep diffusion-weighted imaging reconstruction.
- We achieved navigator-free high-resolution DWI with 21 diffusion-encoding directions at 0.7 mm isotropic resolution, and a scan time of under 10 minutes.

## II. RELATED WORK

### A. Multi-Band Multi-Shot DWI Acquisition & Modeling

Our previous work [35] demonstrated the joint  $k$ - $q$ -slice forward operator for multi-band multi-shot navigator-based interleaved EPI (NAViEPI) DWI acquisition. This operator can be understood as an extended sensitivity encoding (SENSE) operator [11], which maps the multi-slice multi-diffusion-weighted images ( $\tilde{x}$ ) to their corresponding  $k$ -space,

$$\mathcal{A}(\tilde{x}) = \mathbf{P}\Sigma\Theta\mathbf{F}\mathbf{S}\Phi\tilde{x} \quad (1)$$

Here, the images  $\tilde{x}$  are point-wise multiplied with the pre-computed shot-to-shot phase variation maps ( $\Phi$ ) and coil sensitivity maps ( $\mathbf{S}$ ). The output images are then converted to  $k$ -space via two-dimensional fast Fourier transform ( $\mathbf{F}$ ), point-wise multiplied with the multi-band phases ( $\Theta$ ), summed

along the slice dimension ( $\Sigma$ ), and then multiplied by the  $k$ -space undersampling mask ( $\mathbf{P}$ ).

In Equation (1), one challenge is to accurately estimate the shot-to-shot phase variation. Multiplexed sensitivity-encoding (MUSE) type reconstruction techniques [36]–[39] realized the self-gating strategy, where the  $k$ -space data of each shot was used to reconstruct its corresponding shot image followed by a phase smoothing approach. Self-gated shot phase estimation does not require the acquisition of phase navigator data. However, it requires marginal undersampling factors per shot and fully-sampled DWI acquisition assembling all shots. Alternatively, undersampled DWI acquisition can be enabled via the acquisition of navigators for shot phase estimation [35]. This approach allows for mesoscale-resolution DWI at 7 T, but still needs long scan time. As listed in Table I, the total acquisition of Protocol #3 at 0.7 mm isotropic resolution takes 16 : 27 minutes with phase navigators. This scan time can be reduced to approximately 10 minutes by removing the phase navigators (Protocol #4 in Table I).

With the operator  $\mathcal{A}$ , the joint reconstruction is expressed as,

$$\underset{\tilde{x}}{\operatorname{argmin}} \|\mathbf{y} - \mathcal{A}(\tilde{x})\|_2^2 + \lambda \mathcal{R}(\tilde{x}) \quad (2)$$

where  $\mathbf{y}$  is the measured  $k$ -space data. The first term in Equation (2) presents data consistency, and the second term presents the regularization function  $\mathcal{R}(\tilde{x})$  with the regularization strength  $\lambda$ . When using the Tikhonov regularization, i.e.  $\mathcal{R}(\tilde{x}) = \|\tilde{x}\|_2^2$ , Equation (2) can be solved via the conjugate gradient (CG) method. For nonlinear regularization functions, such as the locally-low rank (LLR) regularization [35] or neural networks with nonlinear activation functions, ADMM was employed in this work to solve for Equation (2).

### B. Algorithm Unrolling for Deep Image Reconstruction

Algorithm unrolling has been an emerging technique in solving inverse problems with learnable deep neural networks. Algorithm unrolling consists of two ingredients. First, it uses deep neural networks to learn regularization function. Second, it is constrained by the data-consistency term. In other words, the forward pass of the estimate  $\mathcal{A}(\tilde{x})$  must be close to the measured data  $\mathbf{y}$ . By mapping the operations used in iterative algorithms onto networks, unrolled algorithms can be trained with data, leading to much faster inference than conventional iterative algorithms [26]. Further, recent developments have shown that the operations used in compressed sensing MRI, i.e., sparsifying transformation and soft thresholding, can be learned via neural networks. For instance, Hammernik et al. [27] proposed to unroll the gradient descent algorithm with a learned neural network (e.g. U-net [40]) as the regularization function. Aggarwal et al. [28] proposed the model-based deep learning architecture for inverse problems (MoDL) to unroll the alternating minimization algorithm with a learned residual denoising network [41] as regularization.

### C. Self-Supervised Learning for Image Reconstruction

In many MRI applications, such as dynamic imaging and diffusion-weighted imaging acquiring fully-sampled data for

supervised learning can be challenging. To tackle this issue, Yaman et al. [29] proposed self-supervised learning via data undersampling (SSDU), which learns the regularization function in Equation (2) by splitting available undersampled data into two disjoint sets, one of which is used in the data consistency term and another used for the computation in the training loss function. The training of SSDU requires large undersampled data sets. To close the domain gap between training and test data, Yaman et al. [30] proposed scan-specific zero-shot self-supervised learning (ZSSSL), which splits a single data set into three disjoint sets for (a) the data consistency term, (b) the loss calculation during training, and (c) validation, respectively. Recently, ZSSSL has been adopted for multi-contrast image reconstruction [42].

### III. METHODS

#### A. Data Acquisition

Table I lists four acquisition protocols implemented on a clinical 7 T MR system (MAGNETOM Terra, Siemens Healthineers, Erlangen, Germany) with a 32-channel head coil (Nova Medical, Wilmington, MA, USA) and the XR-gradient system (maximum gradient strength 80 mT/m and a peak slew rate 200 T/m/s). The first protocol employed in-plane fully-sampled four-shot EPI and thus supplied ground truth data for the validation of our proposed methods. The second protocol employed 3-shell diffusion acquisition with  $b$ -values spanning 1000, 2000, and 3000 s/mm<sup>2</sup>. The last two protocols implemented mesoscale 0.7 mm isotropic resolution based on NAViEPI or iEPI with both in-plane and slice acceleration as 2, supplying a total acquisition time of 16 : 27 and 9 : 57 minutes, respectively. Three young healthy volunteers with written informed consent approved by the local ethics committee participated in this study.

#### B. Image Reconstruction via ADMM Unrolling and Zero-Shot Self-Supervised Learning

Instead of the two-step alternating minimization unrolling scheme as used in MoDL [28], we employed the ADMM unrolling to solve the self-supervised learning reconstruction in Equation (2). The update rule of ADMM unrolling reads

$$\begin{cases} \tilde{\mathbf{x}}^{(k+1)} = \underset{\mathbf{x}}{\operatorname{argmin}} \|\mathbf{y} - \mathcal{A}(\mathbf{x})\|_2^2 + \rho/2 \|\mathbf{x} - \mathbf{v}^{(k)} + \mathbf{u}^{(k)}\|_2^2 \\ \mathbf{v}^{(k+1)} = (\lambda/\rho) \cdot \mathcal{D}_\omega(\tilde{\mathbf{x}}^{(k+1)} + \mathbf{u}^{(k)}) \\ \mathbf{u}^{(k+1)} = \mathbf{u}^{(k)} + \tilde{\mathbf{x}}^{(k+1)} - \mathbf{v}^{(k+1)} \end{cases} \quad (3)$$

ADMM updates the variables  $\tilde{\mathbf{x}}$ ,  $\mathbf{v}$ , and  $\mathbf{u}$  in an alternating scheme. It splits the unrolled reconstruction into three steps, as shown in Equation (3) and in the pseudo code of Algorithm 1. First, the updating step for  $\tilde{\mathbf{x}}$  is solved by conjugate gradient. Second, the variable  $\mathbf{v}$  is then updated via the forward pass of the neural network  $\mathcal{D}_\omega$  with the input as the sum of current estimates of  $\tilde{\mathbf{x}}$  and  $\mathbf{u}$ . Third, the variable  $\mathbf{u}$  is updated by adding its current estimate to the difference between  $\tilde{\mathbf{x}}$  and  $\mathbf{v}$ .

As shown in Figure 1, the data sampling mask  $\mathbf{P}$  in ZSSSL [30] is split into three disjoint sets, the training mask  $\mathbf{T}$  for the data consistency term, the training loss mask  $\mathbf{L}$  for the loss

---

#### Algorithm 1 ADMM Unrolling for ZSSSL

---

```

1: Initialization:
2:   split sampling mask  $\mathbf{P}$  into 12 repetitions, each of which
   consists of three disjoint sets  $\mathbf{T}$ ,  $\mathbf{L}$ , and  $\mathbf{V}$ 
3:    $p \leftarrow 0$  and  $N_{\text{epoch}} \leftarrow 100$ 
4:    $\mathcal{D}_\omega$  set as ResNet
5:    $\rho \leftarrow 0.05$  and  $\lambda \leftarrow 0.05$ 
6:    $\text{Loss}_{\text{valid}} \leftarrow \inf$  and  $\text{trace} \leftarrow 0$ 
7:   function ADMM(mask)
8:      $\mathcal{A}_{\text{mask}} \leftarrow$  set the mask in the forward operator  $\mathcal{A}$ 
9:      $\tilde{\mathbf{x}}^{(0)} \leftarrow \mathcal{A}_{\text{mask}}^H(\mathbf{y})$ 
10:     $\mathbf{v}^{(0)} \leftarrow \tilde{\mathbf{x}}^{(0)}$  and  $\mathbf{u}^{(0)} \leftarrow \mathbf{0}$ 
11:     $k \leftarrow 0$  and  $N_{\text{unroll}} \leftarrow 8$ 
12:    while  $k < N_{\text{unroll}}$  do
13:       $\tilde{\mathbf{x}}^{(k+1)} \leftarrow$  conjugate gradient with 6 iterations
14:       $\mathbf{v}^{(k+1)} \leftarrow (\lambda/\rho) \cdot \mathcal{D}_\omega(\tilde{\mathbf{x}}^{(k+1)} + \mathbf{u}^{(k)})$ 
15:       $\mathbf{u}^{(k+1)} \leftarrow \mathbf{u}^{(k)} + \tilde{\mathbf{x}}^{(k+1)} - \mathbf{v}^{(k+1)}$ 
16:       $k \leftarrow k + 1$ 
17:    end while
18:    return  $\tilde{\mathbf{x}}^{(k+1)}$ 
19:  end function
20: Training:
21:  while  $p < N_{\text{epoch}}$  or  $\text{trace} \leq 12$  do
22:     $\mathbf{x}_t \leftarrow \text{ADMM}(\mathbf{T})$ 
23:     $\text{Loss}_{\text{train}} \leftarrow \mathcal{L}(\mathbf{Ly}, \mathcal{A}_{\mathbf{L}}(\mathbf{x}_t))$ 
24:    update  $\omega$  via ADAM
25:    Validation:
26:     $\mathbf{x}_t \leftarrow \text{ADMM}(\mathbf{T} \cup \mathbf{L})$ 
27:     $\text{Loss}_{\text{temp}} \leftarrow \mathcal{L}(\mathbf{Vy}, \mathcal{A}_{\mathbf{V}}(\mathbf{x}_t))$ 
28:    if  $\text{Loss}_{\text{temp}} \leq \text{Loss}_{\text{valid}}$  then
29:       $\text{Loss}_{\text{valid}} \leftarrow \text{Loss}_{\text{temp}}$ 
30:       $\text{trace} \leftarrow 0$ 
31:    else
32:       $\text{trace} \leftarrow \text{trace} + 1$ 
33:    end if
34:  end while

```

---

function calculation, and the validation loss mask  $\mathbf{V}$ . Each set consists of 12 repetitions constructed via random uniform sampling of the data mask  $\mathbf{P}$ . In each training epoch, every repetition is looped through in order to update the ResNet parameters  $\omega$ . Plus, the validation step is performed after every training epoch to update the minimal validation loss. If the validation loss does not reduce for 12 consecutive epochs or if 100 epochs are reached, the training is terminated.

The index  $k$  in Equation (3) denotes the unrolling iteration, and  $\mathcal{D}_\omega$  denotes the residual network (ResNet) [41] parameterized by  $\omega$ . In this work, 2D convolution was employed to construct the ResNet. In PyTorch, 2D convolution requires four-dimensional tensors as input and output. For instance, a matrix with the size  $(N, C, H, W)$  is acceptable for the 'conv2d' function in PyTorch. Here,  $W$  and  $H$  denote the width and height of the convolution kernel,  $C$  denotes the number of channels, and  $N$  denotes the batch size. However, the DWIs ( $\tilde{\mathbf{x}}$ ) to be reconstructed has the size  $(N_{\text{diff}}, N_Z, N_Y, N_X, 2)$ , where 2 stands for the real and imaginary part of the complex-valued DWIs.  $N_X$  and  $N_Y$  are the width and the height of

TABLE I  
IEPI WITH OR WITHOUT NAVIGATORS ACQUISITION PROTOCOLS

Protocol	#1	#2	#3	#4
Diffusion mode			MDDW	
Diffusion scheme			monopolar	
Diffusion direction	20	114		20
b-value (s/mm <sup>2</sup> )	1000	3-shell		1000
$b_0$	1	12		1
FOV (mm <sup>2</sup> )			200	
Matrix size		200 × 200		286 × 286
In-plane resolution (mm <sup>2</sup> )		1.0 × 1.0		0.7 × 0.7
Slice thickness (mm)		1.0		0.7
Slices	141	114		176
Navigator		No	Yes	No
Shots	4	2		3
TR (ms)	7700	4900	15000	8900
TE (ms)	67	70	58/98.3	58
ESP (ms)		1.02		1.17
Bandwidth (Hz/Pixel)		1086		972
Partial Fourier		6/8		5/8
Acceleration	$1 \times 3$	$3 \times 3$		$2 \times 2$
Acquisition (min)	10 : 42	20 : 55	16 : 27	9 : 57

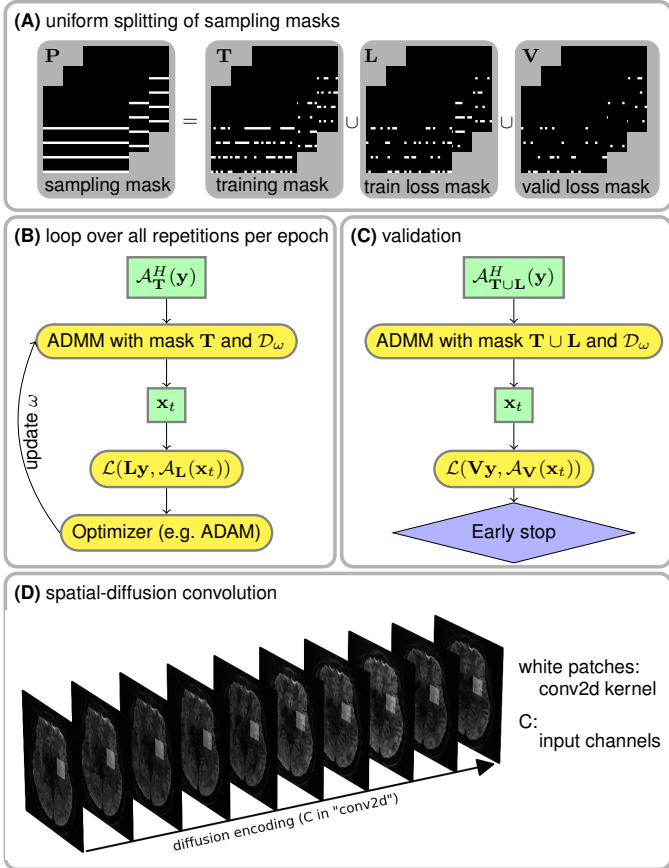


Fig. 1. Illustration of the key components in ZSSSL. (A) The sampling mask  $P$  in Equation (1) was uniformly split into three disjoint sets: the training mask  $T$  used for the data consistency term during ZSSSL training, the train loss mask  $L$  used for the loss function calculation during ZSSSL training, and the validation loss mask  $V$  used for the loss function calculation during ZSSSL validation. (B) and (C) show the flowchart for the training and the validation of ZSSSL, respectively. Note that the ResNet parameters  $\omega$  are updated during training, but remain fixed during the validation step. (D) A stack of DWIs is input into ResNet during ADMM unrolling.

DWIs,  $N_Z$  is the number of slices (same as the multi-band factor), and  $N_{\text{diff}}$  is the number of diffusion encodings. To train a ResNet based on 2D convolution, the DWIs were reshaped and permuted as  $(N_Z, 2 \cdot N_{\text{diff}}, N_Y, N_X)$ , as illustrated in Figure 1 (D). In this manner, 2D convolution kernels in combination with ReLU activation functions loop through the varying diffusion-weighted contrast to learn the key features of the high-dimensional data and to reduce noisy and aliasing artifacts in unrolled reconstruction.

### C. Comparison of Regularization Techniques

In this work, using the 4-shot fully-sampled iEPI [43] data acquired by Protocol #1 from Table I, we compared the reconstruction performance of three different regularization techniques, Tikhonov  $\ell^2$  regularization (as used in MUSE), LLR regularization, and ZSSSL with a learned regularization. Note that MUSE is a simultaneous multi-slice (SMS) parallel imaging method and poses no regularization along the diffusion dimension, effectively solving each DWI reconstruction independently. In contrast, all other regularized reconstructions fall into the joint reconstruction regime. This method jointly reconstructs all DWIs and imposes regularization terms that explore spatial-diffusion redundancy. For example, LLR enforces low rankness of local spatial-diffusion matrices from DWIs, whereas ZSSSL learns a ResNet regularization function based on spatial-diffusion convolution kernels while enforcing data consistency during the unrolled training process.

### D. Self-Gated ZSSSL

As discussed in Section II-A, there are two approaches for estimating shot-to-shot phase variation: self-gated and navigator-based. The self-gated approach, as used in MUSE [38], requires fully-sampled DWI acquisition and has typically reported only a small number of shots (up to 4). The previously proposed NAViEPI approach enabled high-resolution DWI with the use of undersampled iEPI and shot-to-shot phase navigator acquisition. While NAViEPI results in shorter scan

time than fully-sampled iEPI, the use of phase navigator still elongates the acquisition, as listed in Table I. Therefore, a key question is whether it would be feasible to discard phase navigator while keeping undersampled iEPI acquisition. In this work, we investigated the feasibility of ZSSSL in self-gated scan for 0.7 mm isotropic resolution DWI.

### E. ZSSSL Model Generalization

We evaluated the generalization of the ZSSSL model in two aspects. First, using the 4-shot fully-sampled data acquired by Protocol #1 Table I, we trained ZSSSL with all 4 shots and then tested the trained model with retrospectively undersampled 2-shot data. Second, with the 0.7 mm isotropic resolution DWI data containing 88 multi-band slices acquired from Protocol #3 in Table I, we trained the ZSSSL with only one slice and then performed the inference reconstruction on the remaining slices.

### F. Computation

All reconstructions were in this work done on a single A100 SXM4/NVLink GPU with 80 GB memory (NVIDIA, Santa Clara, CA, USA). Computing infrastructure was provided by the Erlangen National High Performance Computing Center.

Note that the data from Protocol #2 in Table I contains a total of 126 diffusion-weighted images, which is too large for the LLR and the ResNet computation in a single A100 GPU. As a result, this data was uniformly split into three consecutive parts, with each part containing 42 diffusion-weighted images.

## IV. RESULTS

### A. Comparison of Regularization Techniques

Figure 2 displays the regularized reconstruction results using both the 4-shot fully-sampled iEPI data and the retrospectively 2-shot undersampled iEPI data. Firstly, compared to MUSE, all other regularized joint reconstructions (LLR and ZSSSL) demonstrated denoising capabilities in the case of 4-shot fully-sampled iEPI. Secondly, when the 4-shot iEPI data was retrospectively undersampled to 2 shots, the undersampling factor became  $4 \times 3$  (4-fold in-plane undersampling and 3-fold slice undersampling). As expected, the MUSE reconstruction showed increased noise. In contrast, both LLR and ZSSSL reconstructions showed strong denoising performance. ZSSSL, in particular, provided sharper and clearer delineation of brain tissues compared to LLR. This may attribute to the fact that the same LLR regularization strength was used for both the 4-shot and the 2-shot reconstructions. While this empirically chosen regularization strength was optimal for the 4-shot data, it resulted in slightly blurring artifacts for the 2-shot data. ZSSSL, on the contrary, learned the regularization strength ( $\lambda$  in Equation (2)) during training, eliminating the need for empirical selection. Moreover, note that the LLR reconstruction took about 40 minutes for the data, whereas the training of ZSSSL required about 3 hours, with inference taking only 1 minute.

### B. DWI at b-Value of 3000 s/mm<sup>2</sup>

Figure 3 compares the LLR and ZSSSL reconstruction results of the 3-shell 1.0 mm isotropic resolution DWI, as acquired by Protocol #2 in Table I. Diffusion-weighted images at the  $b$ -value of 3000 s/mm<sup>2</sup> supplied stronger diffusion weighting as compared to lower  $b$ -values, but this came at the cost of increased noise and blurring. The proposed self-gated ZSSSL was advantageous in regaining signal-to-noise ratio (SNR) and improving structural continuity and sharpness in all orientations.

Figure 4 displays the training and validation loss as well as the learned regularization strength along epochs. It can be seen that 100 epochs were sufficient for the convergence of ADMM unrolling. In addition, the regularization strength converged to the value of 0.02.

### C. Retrospectively Self-Gated ZSSSL

Figure 5 demonstrates the efficacy of the self-gated ZSSSL reconstruction by comparing to the standard navigated LLR regularized reconstruction using the NAViEPI data from Protocol #3 in Table I. The 19th diffusion-encoding (without inter-shot motion) and the 5th diffusion-encoding (with accidental inter-shot motion) reconstruction results were displayed.

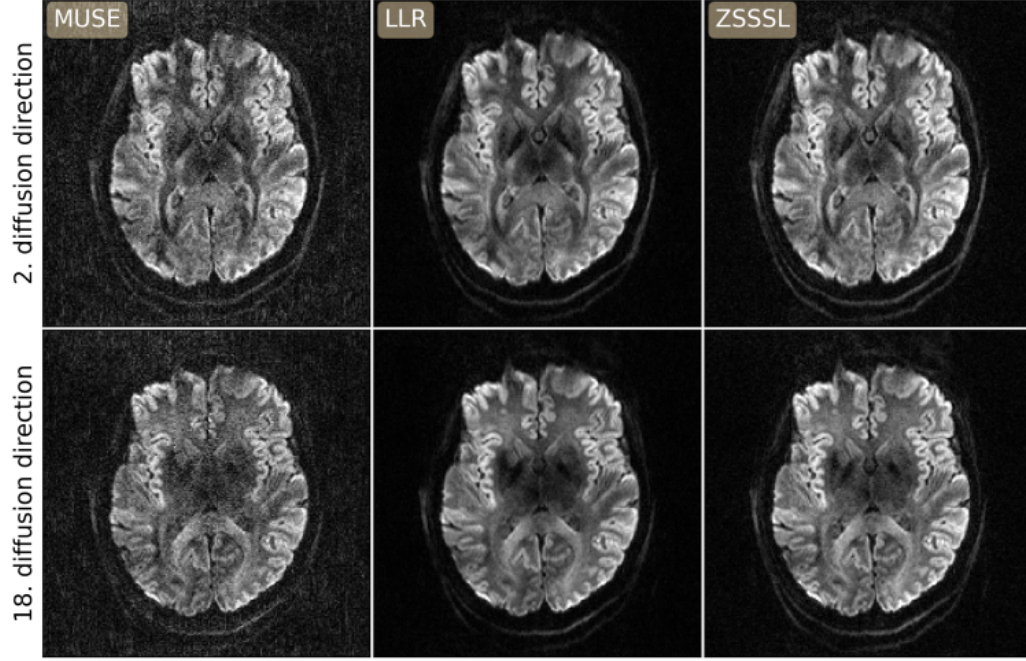
The selected DWIs showed residual aliasing-like and severe motion-blurring artifacts in the navigated LLR reconstruction. The main reason of these artifacts is that the addition of navigator acquisition increased the total scan time, resulting in higher sensitivity to accidental inter-shot motion. Admittedly, navigators are valuable in the case of ultra high resolution using many shots, e.g. 3-fold in-plane undersampling and 5-shot acquisition for the in-plane resolution of 0.5 mm [35]. In this experiment, however, the utilization of 3 shots yielded  $6 \times 2$ -fold acceleration per shot (refer to Protocol #3). Such an acceleration rate proved achievable for the self-gated approach, as demonstrated in the self-gated ZSSSL reconstruction results. The self-gated ZSSSL reconstruction largely reduced the residual aliasing and motion artifact. The phases of the reconstructed DWIs from self-gated ZSSSL were much less and more flattened than those from navigated LLR. This is because of the echo time difference between the imaging and the navigator echoes.

Figure 6 shows diffusion-weighted images at the 11th diffusion encoding (with motion) in the coronal and the sagittal view, respectively. As mentioned in Section III-E, ZSSSL was trained using only one slice and then inferred on the remaining slices. The ZSSSL model generalized well across slices. More importantly, navigated LLR reconstruction suffered from motion-induced stripping artifacts in both coronal and sagittal views [44], whereas the self-gated ZSSSL approach substantially removed such artifacts and supplies high-quality DWI without the need of navigator.

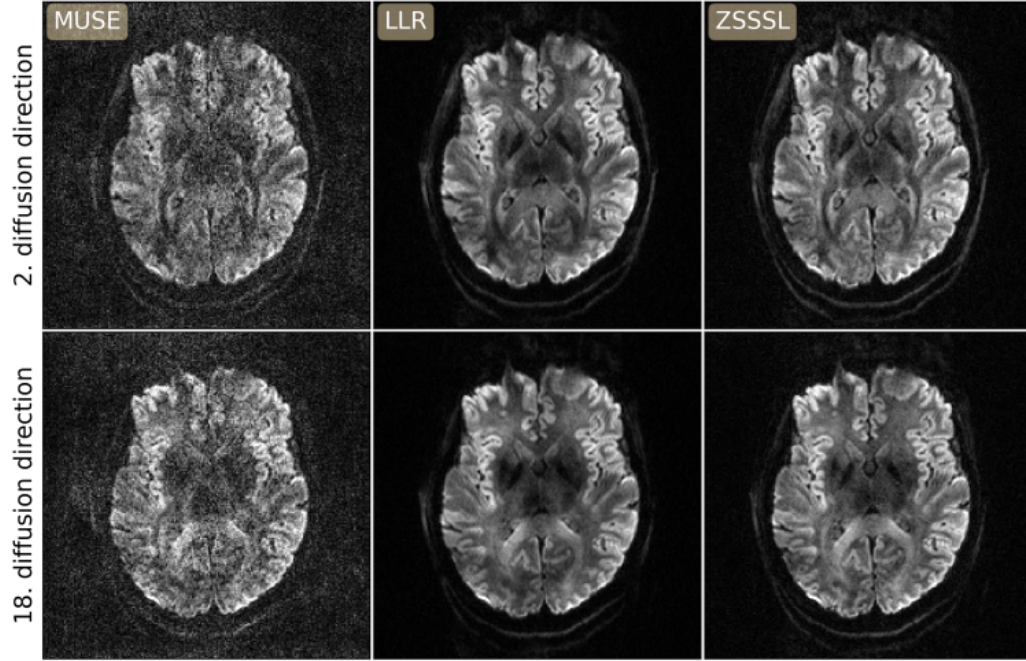
### D. Prospectively Self-Gated ZSSSL

Figure 7 compares the reconstruction results using the prospectively acquired iEPI data without navigator (refer to Protocol #4 in Table I). The snapshot single diffusion-direction DWIs at three orthogonal planes were displayed. The MUSE

(A) 1.0 mm ISO 4-shot fully-sampled iEPI



(B) 1.0 mm ISO 2-shot undersampled iEPI



reconstruction suffered from strong noise at such high spatial resolution. The LLR regularized reconstruction largely reduced noise, but suffered from spatial blurring and signal dropout, as indicated by red arrows in Figure 7. Moreover, even though navigator was not acquired in this experiment, the self-gated LLR approach still showed residual stripping artifacts in the coronal and the sagittal views, as indicated by blue arrows. In contrast, the proposed self-gated ZSSSL approach significantly reduced motion-induced spatial blurring and regained sharp diffusion-weighted contrasts.

## V. DISCUSSION

This work reported a novel self-gated zero-shot self-supervised learning approach for multi-shot undersampled iEPI acquisition and high-resolution DWI reconstruction. The self-gated ZSSSL achieved whole brain diffusion encoding in 21 directions with a  $b$ -value of  $1000 \text{ s/mm}^2$  at  $0.7 \text{ mm}$  isotropic resolution, all within a scan time of less than 10 minutes. Technically, this work unrolled ADMM to perform ZSSSL training and testing. Likewise, ADMM was employed to solve the inverse problem in Equation (2) with LLR regularization. This approach assures fair comparison among different regularization methods.

**Fig. 2.** (A) Comparison of different regularization functions on 1.0 mm isotropic resolution 4-shot fully-sampled iEPI (Protocol #1 in Table I)) 6 DWI reconstruction: (1st column) MUSE with Tikhonov regularization, joint DWI reconstruction with (2nd column) LLR regularization, (3rd column) ZSSSL with ResNet. DWIs from the 2nd and the 18th diffusion-encoding direction were shown. (B) Comparison of the above regularization functions on 1.0 mm isotropic resolution retrospectively 2-shot undersampled iEPI DWI reconstruction. Retrospective undersampling induced more noise in the MUSE reconstruction. Both LLR and ZSSSL demonstrated superior noise reduction. ZSSSL showed sharper and clearer structural delineation in both reconstructions.

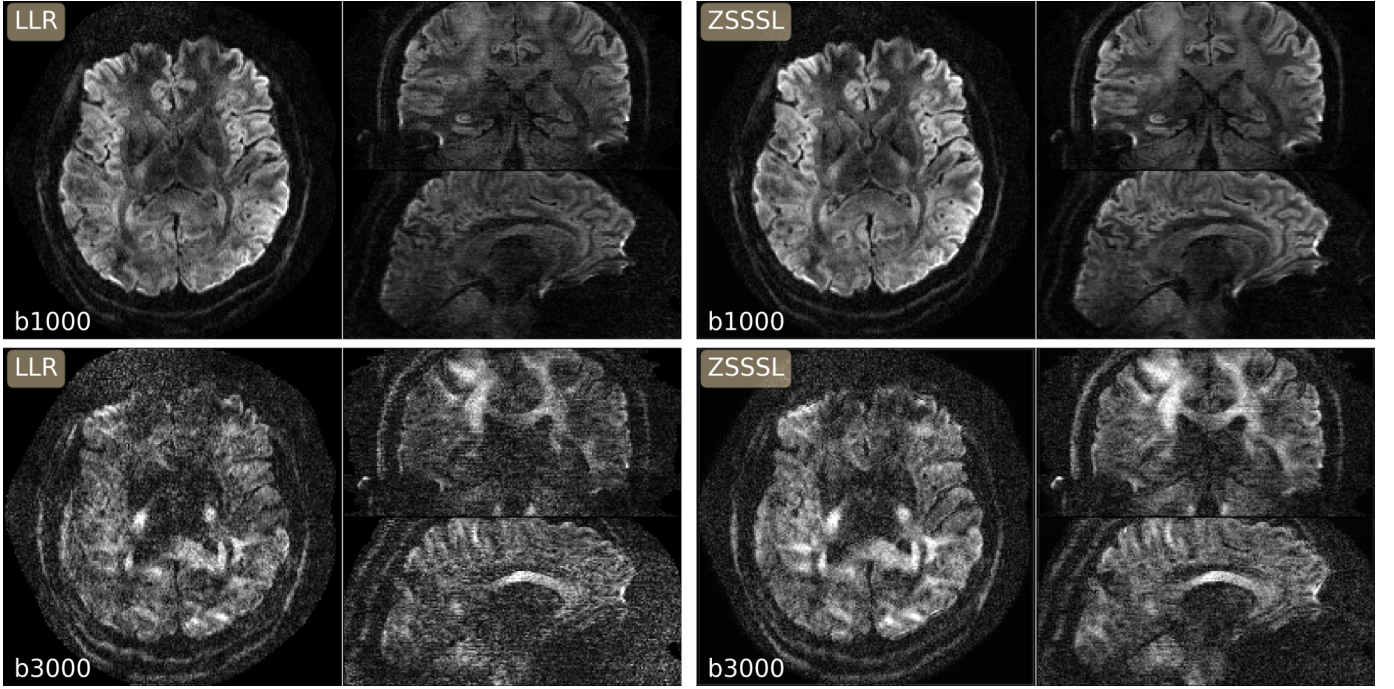


**Fig. 3.** Reconstruction results of 3-shell 1.0 mm isotropic resolution DWI with  $3 \times 3$  acceleration: (left) LLR and (right) ZSSSL. The images are shown in three orthogonal planes for one diffusion-encoding direction at the  $b$ -values of (top) 1000 and (bottom) 3000  $\text{s/mm}^2$ , respectively.

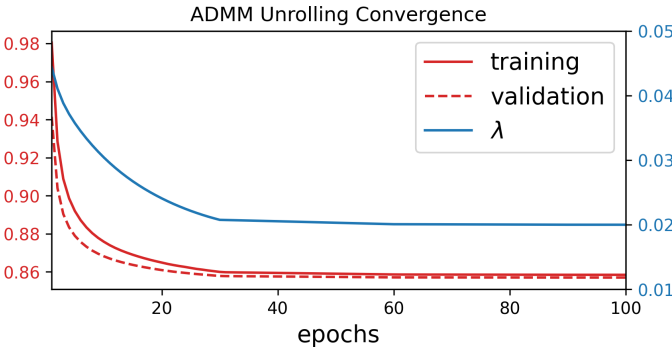


**Fig. 4.** Convergence analysis along the ADMM unrolling training and validation epochs for the ZSSSL results in Figure 3. Displayed curves are (red solid) the training loss, (red dashed) the validation loss, and (blue solid) the learned regularization strength  $\lambda$ , respectively.

The proposed self-gated ZSSSL approach is well-suited for online reconstruction deployment. Firstly, it requires much shorter acquisition time than the conventional MUSE approach with fully-sampled iEPI and our previous NAViEPI method. Secondly, ZSSSL does not require large-scale fully-sampled data for training. Instead, the training of ZSSSL is scan specific. Last but not the least, the trained ZSSSL model is applicable to different undersampling factors and to different slices. Fourth, the inference time of ZSSSL is much shorter compared to the LLR regularization approach.

We observed that stripping-type motion artifacts occurred more frequently with sub-millimeter isotropic resolution DWI. In addition, sub-millimeter isotropic voxel resulted in higher noise in DWI. This makes sense, as scans with reduced slice thickness are more susceptible to shot-to-shot phase variations. To enable sub-millimeter mesoscale DWI, Setsompop et

al. [45] proposed the gSlider technique with slice phase-dither encoding, which excites one slab multiple times with complementary slice encoding schemes. gSlider has been proven effective in alleviating motion sensitivity, because the thicker slab (in comparison to the thin single slice) reduced inter-slice motion. Meanwhile, Hadamard encoding of the slices within a slab gained SNR in the linear inverse reconstruction. However, it has been reported that gSlider has stricter requirements on  $B_0$  and  $B_1$  field homogeneity and shows residual slab boundary blurring [46]. In contrast, the proposed self-gated ZSSSL method requires no such advanced slab encoding, while achieves sub-millimeter resolution at a clinical feasible reconstruction time. Thus, the proposed method can be useful for the probe to high-resolution brain micro-structures in the human connectome project [47].

This work demonstrated the capability of self-gated ZSSSL in reconstructing 0.7 mm isotropic resolution 3-shot iEPI DWI with  $(6 \times 2)$ -fold acceleration per shot. However, we also observed that the self-gated approach failed to recover aliasing-free DWI in the case of higher acceleration factors (e.g. the  $0.5 \times 0.5 \times 2.0 \text{ mm}^3$  DWI data with an acceleration of  $10 \times 2$  per shot). To address this issue, employing optimized trajectories with a more densely-sampled  $k$ -space central region could help better estimate shot phase variations [36], [48].

This work did not incorporate off-resonance correction in the reconstruction. As a logic extension, the multi-shot sequence can be modified to encode dynamic  $B_0$  field variation, which can then be employed in the SENSE-based forward operator and reconstruction. An established approach is known as the blip-up/down encoding [49]. This approach can potentially be combined with the model-based reconstruction for joint reconstructions of DWIs and  $B_0$  field maps [50].

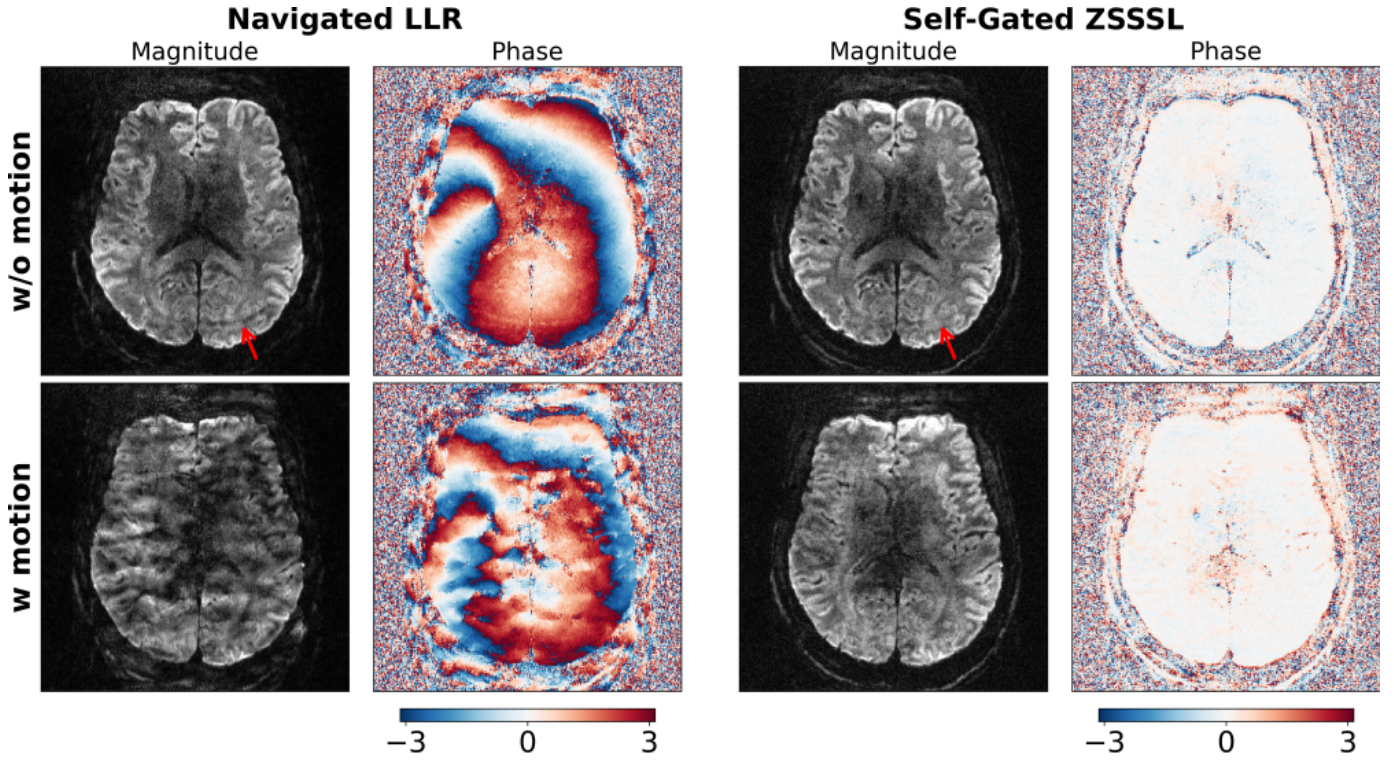


**Fig. 5.** 0.7 mm isotropic resolution DWI reconstruction results based on the NAViEPI data acquired with Protocol #3 in Table I. (Left) LLR regularized reconstruction with shot phase estimated from navigators. (Right) ZSSSL reconstruction with self-gated shot phase estimation. The magnitude and the phase of the 19th-direction (without motion) and the 5th-direction (with motion) DWIs are displayed.

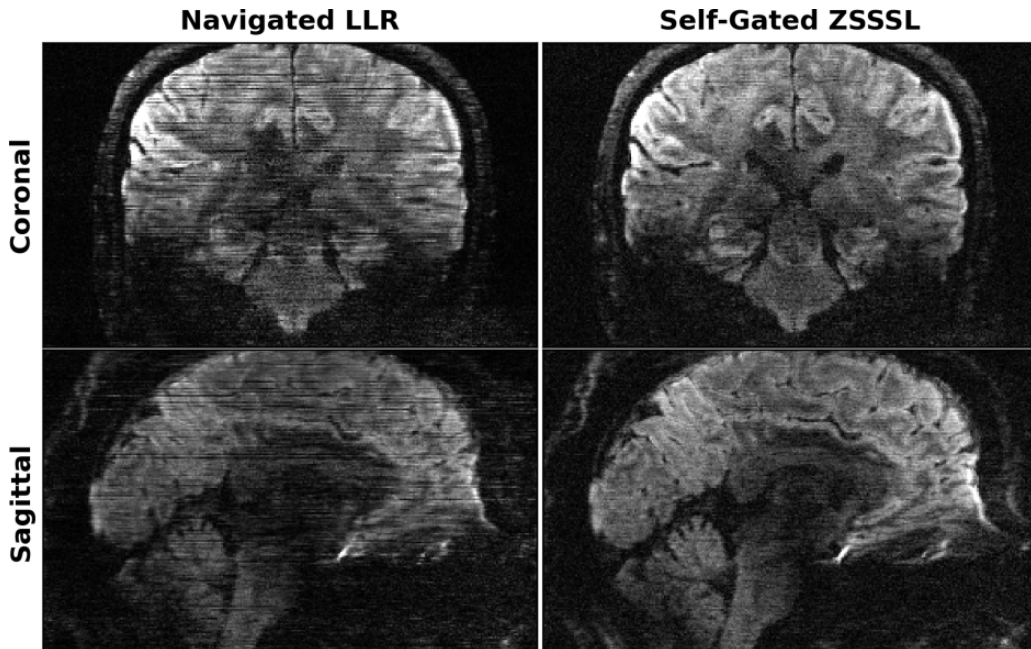


**Fig. 6.** 0.7 mm isotropic resolution DWI of the 11th diffusion encoding (with motion) in (top) the coronal and (bottom) the sagittal orientation, respectively. Displayed results are (left) the navigated LLR regularized and (right) the self-gated ZSSSL reconstruction.

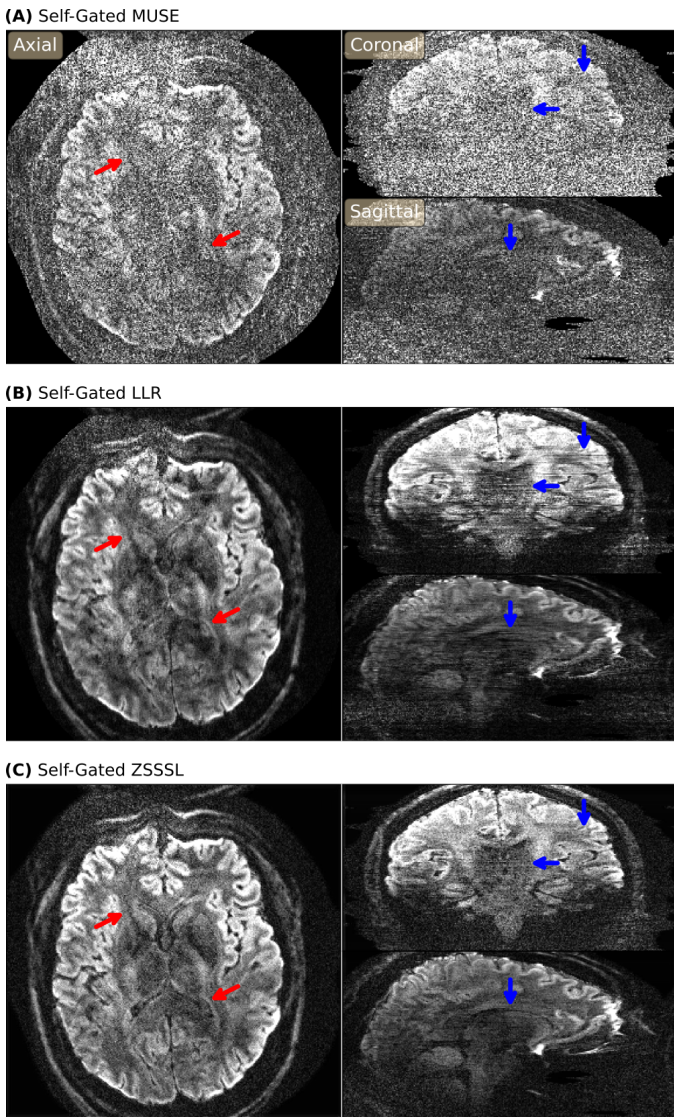


**Fig. 7.** 0.7 mm isotropic resolution DWI of the 11th diffusion encoding (with motion) without the acquisition of navigator. The snapshots in the axial, the coronal and the sagittal views were reconstructed by (A) self-gated MUSE, (B) self-gated LLR, and (C) self-gated ZSSSL, respectively.

## VI. CONCLUSION

In this work, we proposed a self-gated zero-shot self-supervised learning reconstruction framework based on ADMM unrolling for high-resolution and motion-robust DWI.

## REFERENCES

- [1] T. R. Brown, B. M. Kincaid, and K. Ugurbil, “NMR chemical shift imaging in three dimensions,” *Proc. Natl. Acad. Sci. USA*, vol. 79, pp. 3532–3526, 1982.
- [2] D. Le Bihan, E. Breton, D. Lallemand, P. Grenier, E. Cabanis, and M. Laval-Jeantet, “MR imaging of intravoxel incoherent motions: application to diffusion and perfusion in neurologic disorders,” *Radiology*, vol. 161, pp. 401–407, 1986.
- [3] K.-D. Merboldt, W. Hanicke, and J. Frahm, “Self-diffusion NMR imaging using stimulated echoes,” *J. Magn. Reson.*, vol. 64, pp. 479–486, 1985.
- [4] M. Doneva, P. Börnert, H. Eggers, C. Stehning, J. Sénégas, and A. Mertins, “Compressed sensing for magnetic resonance parameter mapping,” *Magn. Reson. Med.*, vol. 64, pp. 1114–1120, 2010.
- [5] D. Ma, V. Gulani, N. Seiberlich, K. Liu, J. L. Sunshine, J. L. Duerk, and M. A. Griswold, “Magnetic resonance fingerprinting,” *Nature*, vol. 495, pp. 187–192, 2013.
- [6] E. O. Stejskal and J. Tanner, “Spin diffusion measurements: Spin echoes in the presence of time-dependent field gradient,” *J. Chem. Phys.*, vol. 42, pp. 288–292, 1965.
- [7] P. Mansfield, “Multi-planar image formation using NMR spin echoes,” *J. Phys. C*, vol. 10, pp. 55–58, 1977.
- [8] P. B. Roemer, W. A. Edelstein, C. E. Hayes, S. P. Souza, and O. M. Mueller, “The NMR phased array,” *Magn. Reson. Med.*, vol. 16, pp. 192–225, 1990.
- [9] D. K. Sodickson and W. J. Manning, “Simultaneous acquisition of spatial harmonics (SMASH): Fast imaging with radiofrequency coil arrays,” *Magn. Reson. Med.*, vol. 38, pp. 591–603, 1997.
- [10] K. P. Pruessmann, M. Weiger, M. B. Scheidegger, and P. Boesiger, “SENSE: Sensitivity encoding for fast MRI,” *Magn. Reson. Med.*, vol. 42, pp. 952–962, 1999.
- [11] K. P. Pruessmann, M. Weiger, P. Börnert, and P. Boesiger, “Advances in sensitivity encoding with arbitrary k-space trajectories,” *Magn. Reson. Med.*, vol. 46, pp. 638–651, 2001.
- [12] M. A. Griswold, P. M. Jakob, R. M. Heidemann, M. Nittka, V. Jellus, J. Wang, B. Kiefer, and A. Haase, “Generalized autocalibrating partially parallel acquisitions (GRAPPA),” *Magn. Reson. Med.*, vol. 47, pp. 1202–1210, 2002.
- [13] M. Lustig, D. Donoho, and J. M. Pauly, “Sparse MRI: The application of compressed sensing for rapid MR imaging,” *Magn. Reson. Med.*, vol. 58, pp. 1182–1195, 2007.
- [14] K. T. Block, M. Uecker, and J. Frahm, “Undersampled radial MRI with multiple coils: Iterative image reconstruction using a total variation constraint,” *Magn. Reson. Med.*, vol. 57, pp. 1186–1098, 2007.
- [15] Z.-P. Liang, “Spatiotemporal imaging with partially separable functions,” in *4th IEEE International Symposium on Biomedical Imaging: From Nano to Macro (ISBI’04)*, 2007, pp. 988–991.
- [16] J.-F. Cai, E. J. Candès, and Z. Shen, “A singular value thresholding algorithm for matrix completion,” *SIAM. J. Optim.*, vol. 20, pp. 1956–1982, 2010.
- [17] C. Huang, C. G. Graff, E. W. Clarkson, A. Bilgin, and M. I. Altbach, “ $T_2$  mapping from highly undersampled data by reconstruction of principal component coefficient maps using compressed sensing,” *Magn. Reson. Med.*, vol. 67, pp. 1355–1366, 2012.
- [18] F. Lam and Z.-P. Liang, “A subspace approach to high-resolution spectroscopic imaging,” *Magn. Reson. Med.*, vol. 71, pp. 1349–1357, 2014.
- [19] D. F. McGivney, E. Pierre, D. Ma, Y. Jiang, H. Saybasili, V. Gulani, and M. A. Griswold, “SVD compression for magnetic resonance fingerprinting in the time domain,” *IEEE Trans. Med. Imaging*, vol. 33, pp. 2311–2322, 2014.
- [20] J. I. Tamir, M. Uecker, W. Chen, P. Lai, M. T. Alley, S. S. Vasanawala, and M. Lustig, “ $T_2$  shuffling: Sharp, multicontrast, volumetric fast spin-echo imaging,” *Magn. Reson. Med.*, vol. 77, pp. 180–195, 2017.
- [21] G. E. Hinton and R. R. Salakhutdinov, “Reducing the dimensionality of data with neural networks,” *Science*, vol. 313, pp. 504–507, 2006.
- [22] F. Lam, Y. Li, and X. Peng, “Constrained magnetic resonance spectroscopic imaging by learning nonlinear low-dimensional models,” *IEEE Trans. Med. Imaging*, vol. 39, pp. 545–555, 2019.
- [23] M. Mani, V. A. Magnotta, and M. Jacob, “qModeL: A plug-and-play model-based reconstruction for highly accelerated multi-shot diffusion MRI using learned priors,” *Magn. Reson. Med.*, vol. 86, pp. 835–851, 2021.
- [24] S. Boyd, N. Parikh, E. Chu, B. Peleato, and J. Eckstein, “Distributed optimization and statistical learning via the alternating direction method of multipliers,” *Foundations and Trends in Machine Learning*, vol. 3, pp. 1–122, 2010.
- [25] K. Gregor and Y. LeCun, “Learning fast approximations of sparse coding,” in *27th International Conference on Machine Learning (ICML’27)*, 2010, pp. 399–406.
- [26] V. Monga, Y. Li, and Y. C. Eldar, “Algorithm Unrolling: Interpretable, Efficient Deep Learning for Signal and Image Processing,” *IEEE Signal Processing Magazine*, vol. 38, pp. 18–44, 2021.
- [27] K. Hammernik, T. Klatzer, E. Kobler, M. P. Recht, D. K. Sodickson, T. Pock, and F. Knoll, “Learning a variational network for reconstruction of accelerated MRI data,” *Magn. Reson. Med.*, vol. 79, pp. 3055–3071, 2018.
- [28] H. K. Aggarwal, M. P. Mani, and M. Jacob, “MoDL: Model-based deep learning architecture for inverse problems,” *IEEE Trans. Med. Imaging*, vol. 38, pp. 394–405, 2018.

- [29] B. Yaman, S. A. H. Hosseini, S. Moeller, J. Ellermann, K. Uğurbil, and M. Akçakaya, "Self-supervised learning of physics-guided reconstruction neural networks without fully sampled reference data," *Magn. Reson. Med.*, vol. 84, pp. 3172–3191, 2020.
- [30] B. Yaman, S. A. H. Hosseini, and M. Akçakaya, "Zero-shot self-supervised learning for MRI reconstruction," in *10th International Conference on Learning Representations (ICLR'10)*, 2022.
- [31] F. Knoll, J. Zboncar, A. Sriram, M. J. Muckley, M. Bruno, A. Defazio, M. Parente, K. J. Geras, J. Katsnelson, H. Chandarana, Z. Zhang, M. Drozdzalv, A. Romero, M. Rabbat, P. Vincent, J. Pinkerton, D. Wang, N. Yakubova, E. Owens, C. L. Zitnick, M. P. Recht, D. K. Sodickson, and Y. W. Lui, "fastMRI: A Publicly Available Raw k-Space and DICOM Dataset of Knee Images for Accelerated MR Image Reconstruction Using Machine Learning," *Radiology: Artificial Intelligence*, vol. 2, p. e190007, 2020.
- [32] F. Liu, R. Kijowski, G. E. Fakhri, and L. Feng, "Magnetic resonance parameter mapping using model-guided self-supervised deep learning," *Magn. Reson. Med.*, vol. 85, pp. 3211–3226, 2021.
- [33] Y. Arefeen, J. Xu, M. Zhang, Z. Dong, F. Wang, J. White, B. Bilgic, and E. Adalsteinsson, "Latent signal models: Learning compact representations of signal evolution for improved time-resolved, multi-contrast MRI," *Magn. Reson. Med.*, vol. 90, pp. 483–501, 2023.
- [34] P. J. Basser, J. Mattiello, and D. Le Bihan, "MR diffusion tensor spectroscopy and imaging," *Biophys. J.*, vol. 66, pp. 259–267, 1994.
- [35] Z. Tan, P. A. Liebig, R. M. Heidemann, F. B. Laun, and F. Knoll, "Accelerated diffusion-weighted magnetic resonance imaging at 7 T: Joint reconstruction for shift-encoded navigator-based interleaved echo planar imaging (JETS-NAViEPI)," *Imaging Neuroscience*, vol. 2, pp. 1–15, 2024.
- [36] C. Liu, R. Bammer, D.-h. Kim, and M. E. Moseley, "Self-navigated interleaved spiral (SNAILS): Application to high-resolution diffusion tensor imaging," *Magn. Reson. Med.*, vol. 52, pp. 1388–1396, 2004.
- [37] M. Uecker, A. Karaus, and J. Frahm, "Inverse reconstruction method for segmented multishot diffusion-weighted MRI with multiple coils," *Magn. Reson. Med.*, vol. 62, pp. 1342–1348, 2009.
- [38] N.-K. Chen, A. Guidon, H.-C. Chang, and A. W. Song, "A robust multishot scan strategy for high-resolution diffusion weighted MRI enabled by multiplexed sensitivity-encoding (MUSE)," *NeuroImage*, vol. 72, pp. 41–47, 2013.
- [39] A. Merrem, S. Hofer, A. S. A. Hosseini, D. Voit, K.-D. Merboldt, Z. Tan, and J. Frahm, "Diffusion-weighted MRI of the prostate without susceptibility artifacts: Undersampled multi-shot turbo-STEAM with rotated radial trajectories," *NMR Biomed.*, vol. 32, p. e4074, 2019.
- [40] O. Ronneberger, P. Fischer, and T. Brox, "U-Net: Convolutional Networks for Biomedical Image Segmentation," in *18th International Conference on Medical Image Computing and Computer-Assisted Intervention (MICCAI'18)*, 2015, pp. 234–241.
- [41] K. He, X. Zhang, S. Ren, and J. Sun, "Deep residual learning for image recognition," in *IEEE Conference on Computer Vision and Pattern Recognition (CVPR'16)*, 2016, pp. 770–778.
- [42] A. Heydari, A. Ahmadi, T. H. Kim, and B. Bilgic, "Joint MAPLE: Accelerated joint  $T_1$  and  $T_2^*$  mapping with scan-specific self-supervised networks," *Magn. Reson. Med.*, 2024.
- [43] K. Butts, S. J. Riederer, R. L. Ehman, R. M. Thompson, and C. R. Jack, "Interleaved echo planar imaging on a standard MRI system," *Magn. Reson. Med.*, vol. 31, pp. 67–72, 1993.
- [44] W.-T. Chang, K. M. Huynh, P.-T. Yap, and W. Lin, "Navigator-Free Submillimeter Diffusion MRI using Multishot-encoded Simultaneous Multi-slice (MUSIJUM) Imaging," in *Proceedings of the 29th Annual Meeting of ISMRM*, 2021, p. 1322.
- [45] K. Setsompop, Q. Fan, J. Stockmann, B. Bilgic, S. Huang, S. F. Cauley, A. Nummenmaa, F. Wang, Y. Rathi, T. Witzel, and L. L. Wald, "High-resolution in vivo diffusion imaging of the human brain with generalized slice dithered enhanced resolution: Simultaneous multislice (gSlider-SMS)," *Magn. Reson. Med.*, vol. 79, pp. 141–151, 2018.
- [46] E. Dai, S. Liu, and H. Guo, "High-resolution whole-brain diffusion MRI at 3T using simultaneous multi-slab (SMSlab) acquisition," *NeuroImage*, vol. 237, p. 118099, 2021.
- [47] S. Y. Huang, T. Witzel, B. Keil, A. Scholz, M. Davids, P. Dietz, E. Rumkert, R. Ramb, J. E. Kirsch, A. Yendiki, Q. Fan, Q. Tian, G. Ramos-Llordén, H.-H. Lee, A. Nummenmaa, B. Bilgic, K. Setsompop, F. Wang, A. V. Avram, M. Komlosh, D. Benjamini, K. N. Magdoom, S. Pathak, W. Schneider, D. S. Novikov, E. Fieremans, S. Toumekti, C. Mekkaoui, J. Augustinack, D. Berger, A. Shapson-Coe, J. Lichtman, P. J. Basser, L. L. Wald, and B. R. Rosen, "Connectome 2.0: Developing the next-generation ultra-high gradient strength human MRI scanner for bridging studies of the micro-, meso- and macro-connectome," *NeuroImage*, vol. 243, p. 118530, 2021.
- [48] E. Dai, P. K. Lee, Z. Dong, F. Fu, K. Setsompop, and J. A. McNab, "Distortion-free diffusion imaging using self-navigated Cartesian echo-planar time resolved acquisition and joint magnitude and phase constrained reconstruction," *IEEE Trans Med Imaging*, vol. 41, pp. 63–74, 2022.
- [49] B. Zahneisen, M. Aksoy, J. Maclarens, C. Wuerslin, and R. Bammer, "Extended hybrid-space SENSE for EPI: Off-resonance and eddy current corrected joint interleaved blip-up/down reconstruction," *NeuroImage*, vol. 153, pp. 97–108, 2017.
- [50] a. Tan, C. Unterberg-Buchwald, M. Blumenthal, N. Scholand, P. Schaten, C. Holme, X. Wang, D. Raddatz, and M. Uecker, "Free-breathing liver fat,  $R_2^*$  and  $B_0$  field mapping using multi-echo radial FLASH and regularized model-based reconstruction," *IEEE Transactions on Medical Imaging*, 2022.